

Silicas of Unimodal and Bimodal Porosities Probed by  $^{129}\text{Xe}$  NMR SpectroscopyAnne Davidson<sup>\*,†,§</sup> Patrick Berthault<sup>‡,§</sup> and Hervé Desvaux<sup>‡,§</sup>

Université Pierre et Marie Curie, Réactivité de Surface, UMR 7609, 4 Place Jussieu, 75252 Paris Cedex 05, France, and Laboratoire commun de RMN, DSM/DRECAM/Service de Chimie Moléculaire, URA CEA-CNRS 331, CEA/Saclay, 91191 Gif sur Yvette, France

Received: May 2, 2003; In Final Form: October 8, 2003

A combination of  $^{129}\text{Xe}$  NMR measurements performed at different temperatures gives insight into the surface properties of an MCM-41 of unimodal porosity and of two SBA-15 silicas of bimodal porosity synthesized with (SBA-B) and without (SBA-A) a 373 K hydrothermal treatment. The signatures of xenon located either in disordered intrawall micropores or in mesopore surface defects are distinguished through the study of the temperature of xenon condensation. Even though the volume of micropores is reduced by hydrothermal treatment by nearly 60%, the remaining micropores could be very important to understand the sorption properties of SBA silicas because either their geometry or the hydrophobic character of their surface changes upon hydrothermal treatment.

## Introduction

Because of their specific surface area (larger than  $500\text{ m}^2\cdot\text{g}^{-1}$ ) and their large monodisperse mesopores (diameters larger than  $20\text{ Å}$ ), MCM-41 and SBA-15 mesoporous silicas have been tested for applications such as sorption (for heavy metals<sup>1</sup> or proteins<sup>2</sup>) and supports for electronic or magnetic devices.<sup>3</sup> Although they lack intrinsic catalytic activity in their silica form, they can be functionalized by incorporation of heteroelements such as aluminum for acidic<sup>4</sup> or titanium for redox<sup>5</sup> properties. Their porosity has also been exploited for the nanocasting of metallic<sup>6</sup> and oxide<sup>7</sup> nanowires. The rising importance of these silicas in many fields, particularly for catalysis or separation processes, motivates fundamental studies aimed at understanding and comparing their surface properties.

MCM-41 and SBA-15 silicas are both obtained by supramolecular templating. Despite formal analogies, their synthesis conditions actually differ by the nature of the organic templates (cationic surfactants and neutral triblock copolymers, respectively) and by pH conditions (basic for conventional MCM-41 synthesis<sup>8</sup> and acidic for SBA-15<sup>9</sup>). In addition, the preparation of SBA-15 silicas often involves a hydrothermal treatment applied before template removal. This treatment aims at increasing the mesopore diameter and the compactness of the silica wall by decreasing the wall thickness.<sup>9–15</sup> Another important difference is that, after template removal, the porosity of a conventional MCM-41 is unimodal and made of a 2D hexagonal array of noninterconnected mesopores whereas the porosity of an SBA-15 is more complex and contains an additional microporosity.<sup>10–18</sup> This microporosity, first suggested by carbon and platinum replication experiments,<sup>10,15</sup> has been confirmed by  $\text{N}_2$ <sup>10–12,14</sup> and Ar sorption<sup>15</sup> analysis, by modeling of X-ray diffraction (XRD) intensities,<sup>17</sup> and by high-resolution transmission electron microscopy (TEM).<sup>18</sup> The micropores are embedded within the silica walls and are not directly detected

by XRD because they are disordered. Their diameters are altered at the hydrothermal treatment temperature.<sup>14,15</sup> At high temperature, typically above 373 K, the micropores that connect neighboring mesopores are large enough to be observed by platinum replication experiments. Indeed, after silica dissolution, solid bridges between adjacent platinum nanowires formed in mesopores, can be seen in TEM.<sup>15</sup> These additional micropores are thought to explain why SBA-15 silicas reversibly adsorb short-chain hydrocarbons with a higher selectivity for unsaturated ethylene and propylene than for the corresponding alkanes.<sup>19</sup> In this context, obtaining more detailed information about the characteristics (roughness, distribution of hydrophilic/hydrophobic adsorption sites) of the silica surfaces in mesopores and additional micropores appears crucial.

In the present work,  $^{129}\text{Xe}$  NMR is used to probe and compare the silica surfaces of an MCM-41 of unimodal porosity and two SBA-15 of bimodal porosity synthesized with (SBA-B) and without (SBA-A) hydrothermal treatment at  $100\text{ °C}$ . The high polarizability of the electronic cloud of the xenon atom makes it sensitive to its environment, particularly in porous solids.<sup>20–24</sup> Most of the  $^{129}\text{Xe}$  NMR studies reported so far dealt with zeolites and led to correlations between the  $^{129}\text{Xe}$  chemical shift and the size and shape of zeolitic cavities, or even the electric fields due to cationic sites.<sup>21</sup> The first attempts to extend these general rules to materials with larger pores, even purely siliceous ones, have failed because of the coexistence of xenon adsorbed on inorganic walls and gaseous xenon located either inside (structural porosity) or between (textural porosity) silica grains.<sup>22</sup> However, recent articles<sup>23,24</sup> have revealed that  $^{129}\text{Xe}$  chemical shift variations in mesoporous silicas can be explained by assuming fast interparticle exchange and van der Waals interactions at the surface. The mesopore diameters can then be empirically derived because smaller pores are generally associated with higher chemical shifts. In addition, Terskikh et al.<sup>24</sup> have significantly affected the  $^{129}\text{Xe}$  chemical shift values by incorporating organosilicates, which generate defects such as partially hydrolyzed  $\text{C}(\text{OH})\text{Si}(\text{OSi})_2$  and  $\text{C}(\text{OH})_2\text{Si}(\text{OSi})$  groups, within the silica walls. Similarly, the goal of the present study is to use  $^{129}\text{Xe}$  NMR to compare MCM-41 and SBA-15 silicas

\* Author for correspondence.

† Université Pierre et Marie Curie.

§ E-mail addresses: davidson@ccr.jussieu.fr; pberthault@cea.fr; hdesvaux@cea.fr.

‡ Laboratoire commun de RMN.

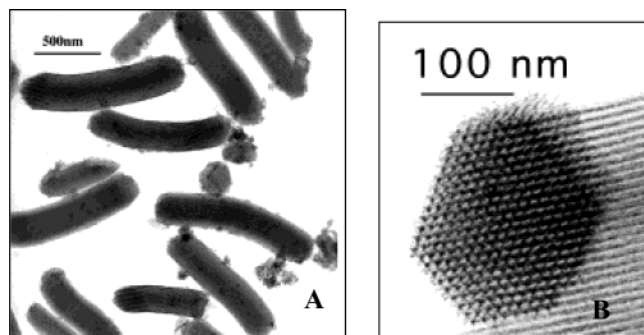


**Figure 1.** Typical TEM images of SBA-B silica: (A) several silica grains with their main axis perpendicular to the electron beam; (B) a single grain with its main axis nearly parallel to the electron beam (honeycomb structure).

**TABLE 1: Structural Properties of the Calcined MCM-41, SBA-A, and SBA-B Silicas Used in the Present Study Extracted from Analysis of TEM, XRD, and  $\text{N}_2$  Sorption Data<sup>a</sup>**

sample	$L$ ( $\mu\text{m}$ )/ $l$ (nm)	$a$ ( $\text{\AA}$ )	$V$ ( $\text{cm}^3\cdot\text{g}^{-1}$ )	$S^*$ ( $\text{m}^2\cdot\text{g}^{-1}$ )	$4V/S^*$ ( $\text{\AA}$ )	$D_{\text{BJH}}$ ( $\text{\AA}$ )
MCM-41	1–2/100–250	44	0.81	1040	29	30
SBA-A	1–2/100–400	95	0.73	750	32	40
SBA-B	1–2/100–350	105	1.23	650	63	65

<sup>a</sup> Length,  $L$ , and diameter,  $l$ , of the silica grains as obtained by TEM. Unit cell parameters,  $a$ , obtained by XRD. Specific surface area,  $S^*$ , measured from  $\text{N}_2$  sorption isotherm at  $P/P_0$  ranging between 0.05 and 0.25, assuming that each  $\text{N}_2$  molecule covers an average surface of  $13.5 \text{ \AA}^2$ . Overall porous volume,  $V$ , at  $P/P_0 = 0.995$ . Mesopore diameter obtained by using the geometrical relation  $4V/S^*$  and mesopore diameter,  $D_{\text{BJH}}$ , using the Barrett–Joyner–Halenda model applied to the desorption branch of the isotherm (maximum of the mesopore diameters distribution curve).

by focusing on the effect of the intrawall micropores on NMR parameters. Because fast intraparticle and interparticle exchange average the information at room temperature, NMR spectra were mainly acquired at low temperature to reduce xenon diffusion and exchange rates and to probe local heterogeneities of the silica surfaces. In the experimental conditions used, the different silica surfaces are clearly distinguished in terms of geometry and adsorption potentials.

## Experimental Section

**Materials.** MCM-41 was synthesized from a basic ammonia solution and templated by cetylammmonium bromide.<sup>8</sup> SBA-A and SBA-B were prepared in an acidic aqueous solution (HCl) and templated by a triblock copolymer (Pluronic, BASF,  $\text{EO}_{20}\text{-PO}_{70}\text{EO}_{20}$ ).<sup>9</sup> After 24 h of synthesis at 310 K, SBA-A was filtered and then calcined at 773 K during 6 h. SBA-B was obtained in similar conditions, but an intermediate hydrothermal treatment of 72 h at 373 K was applied before calcination. The silicas were characterized by TEM. Typical images of the silica grains of the SBA-B powder are shown in Figure 1. Their main structural properties characterized through XRD and  $\text{N}_2$  sorption are given in Table 1. The mesopore diameters, measured on TEM images, are not considered here because it has been shown that the defocus modifies the silica wall thickness and the apparent mesopore diameter.<sup>25</sup> The  $4V/S^*$  and  $D_{\text{BJH}}$  diameter values of MCM-41 are nearly identical, confirming the absence of micropores in this sample. In contrast, the  $D_{\text{BJH}}$  and the  $4V/S^*$  values for SBA-A and SBA-B are significantly different. They are indicated for comparison purpose only because the two models are known to be unreliable in the simultaneous presence of micropores and mesopores.<sup>11,14</sup> The high-pressure

parts of their  $\text{N}_2$  sorption isotherms indicate that the three powders do not contain textural porosity. Before NMR experiments, the three powders were carefully dehydrated (673 K during 6 h under dehydrated air followed by 3 h under argon).

**Methods and Procedures.** The use of laser-polarized xenon recently introduced in the literature for mesoporous silicas<sup>26,27</sup> and silica films<sup>28</sup> and available in our laboratory was found unnecessary. First, the spin–lattice relaxation is relatively fast (on the order of 0.1 Hz), which does not ensure complete description of the porosity.<sup>23</sup> Second, the Boltzmann polarization increases at low temperature and thus enables easy observation of adsorbed xenon, even at moderate pressure.

The dehydrated silica powders (0.1 g) were closely packed to a bed length of about 10 mm in 5 mm-diameter NMR tubes. The NMR tubes were loaded with 4 bar of xenon and 0.7 bar of helium (used to ensure proper thermal contact, even at low temperature<sup>29</sup>) before being flame sealed. This xenon loading corresponds to a surface coverage of  $60 \text{ m}^2$  (assuming a square packing of spherical xenon atoms) and therefore to less than one layer, according to the specific surface areas given in Table 1 (coverage factors of 0.6, 0.8, and 0.9 on MCM-41, SBA-A, and SBA-B, respectively). A reference tube containing only gaseous xenon and helium was also prepared and used for assessing the temperature of xenon phase transition in our experimental conditions. Xenon freezes at 158 K under a pressure of 0.7 atm<sup>30</sup> and at 161 K under 1 atm.<sup>31,32</sup> Because our experiments are run in sealed NMR tubes, the condensation of xenon leads to a pressure drop and consequently changes the temperature of xenon liquefaction. In our reference tube, gaseous xenon is still detected at 170 K, whereas a single line at 288 ppm, assigned to solid xenon, is observed at 159 K (see Supporting Information, Figure S1). This defines the range of temperature at which xenon is liquefied in the absence of silica.

The NMR spectra were recorded on a Bruker DRX-500 spectrometer (magnetic field 11.7 T,  $^{129}\text{Xe}$  Larmor frequency 138.3 MHz) using a 5 mm Nalorac broadband probe head. For the experiments at low temperature, an external liquid nitrogen Dewar in which an electric current vaporizes cold nitrogen toward the probe was used. In the first set of experiments (method A), the sample temperature was decreased slowly from 300 to 155 K in a dynamic mode. Temperature was monitored via a thermocouple located in the probe,  $\sim 1 \text{ cm}$  below the sample. This configuration induced a systematic bias on the temperature, which depended upon the nitrogen gas flow. Therefore, the sample temperature was estimated from the  $^1\text{H}$  NMR spectra of a methanol tube cooled using the same dynamic procedure. In the second set of experiments (method B), absolute temperature calibration was obtained thanks to an independent thermocouple introduced within the magnet in an NMR tube. Two-dimensional chemical exchange NMR experiments (EXSY) were performed with different mixing times and temperatures in the range 170–205 K.<sup>33</sup>

The reported  $^{129}\text{Xe}$  chemical shifts were referenced to the xenon gas peak calibrated to zero at the lowest xenon pressure, that is, at 155 K, and after having checked that the field drift of the spectrometer is lower than 0.1 Hz/h.

## Results and Discussion

At room temperature, the  $^{129}\text{Xe}$  NMR spectra of MCM-41, SBA-A, and SBA-B silicas only exhibit a single symmetrical resonance of chemical shift 65, 95, and 75 ppm, respectively (in addition to that of gaseous xenon present outside the silica grains). The value observed on MCM-41 is consistent with the one recently reported by A. Nossov et al.<sup>27</sup> for a compressed

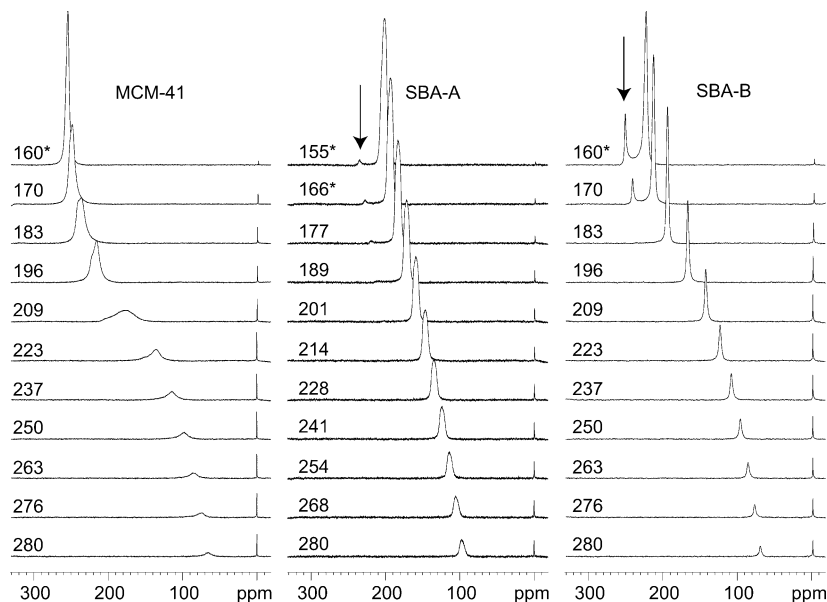


**Figure 2.** Variable temperature  $^{129}\text{Xe}$  NMR spectra of MCM-41, SBA-A, and SBA-B silicas (temperature calibration via a methanol tube, method A). The arrows indicate the small peak assigned to xenon condensed in micropores. The \* symbols correspond to less precisely measured temperatures.

parent silica (70 ppm at room temperature under 0.5 Torr of hyperpolarized xenon). This confirms that the chemical shift of xenon adsorbed on a MCM-41 silica measured at room temperature does not vary significantly with pressure. The value obtained on an SBA-15 silica submitted to a hydrothermal treatment differs from the one reported here for SBA-B, most probably because of significant differences in synthesis conditions (3 h of evolution at room temperature instead of 24 h here, hydrothermal treatment at 373 K for 48 h instead of 72 h here). As expected from the mesopore diameters of SBA-A and SBA-B, the chemical shift of the former is the highest. However, the chemical shift of MCM-41 does not follow the same trend, indicating that the chemical shift is not simply correlated with the mesopore diameter, an observation already reported.<sup>24,26</sup>

Figure 2 displays the  $^{129}\text{Xe}$  NMR spectra of the three silicas recorded between 280 and 155 K (cooling with method A). Above 190 K, a single resonance is observed. Its chemical shift increases as temperature decreases, indicating either an increase of the xenon concentration within the pores or an increase of xenon/surface or xenon/xenon interactions or both. At low temperature ( $T < 190$  K), a single peak remains for MCM-41 whereas two well-resolved peaks are observed for both SBA-A and SBA-B. These two peaks are labeled main and small resonances hereafter, because the integrated intensity of the small one never exceeds 6% of the main resonance intensity in the spectra that we have collected. The following analysis therefore distinguishes the behavior of the main peak, observed for MCM-41, SBA-A, and SBA-B, and that of the small peak, which is specifically observed for SBA-A and SBA-B. At that point, it is important to stress that, at 170 K, the small and main peaks of the two SBA-15 silicas are associated with coexisting adsorption sites experiencing a rather fast exchange. Indeed, cross-peaks are observed on 2D EXSY spectra (illustrated for SBA-A in Supporting Information, Figure S2) for a mixing time of 60 ms.

**Single Peak of MCM-41 and Main Peaks of SBA-A and SBA-B Silicas.** Figure 3 shows the dependence with temperature of chemical shift and integrated intensity of these peaks, extracted from the spectra shown in Figure 2. For the three silicas, the two parameters increase when temperature decreases. The slopes of the intensity curves, observed for MCM-41 and

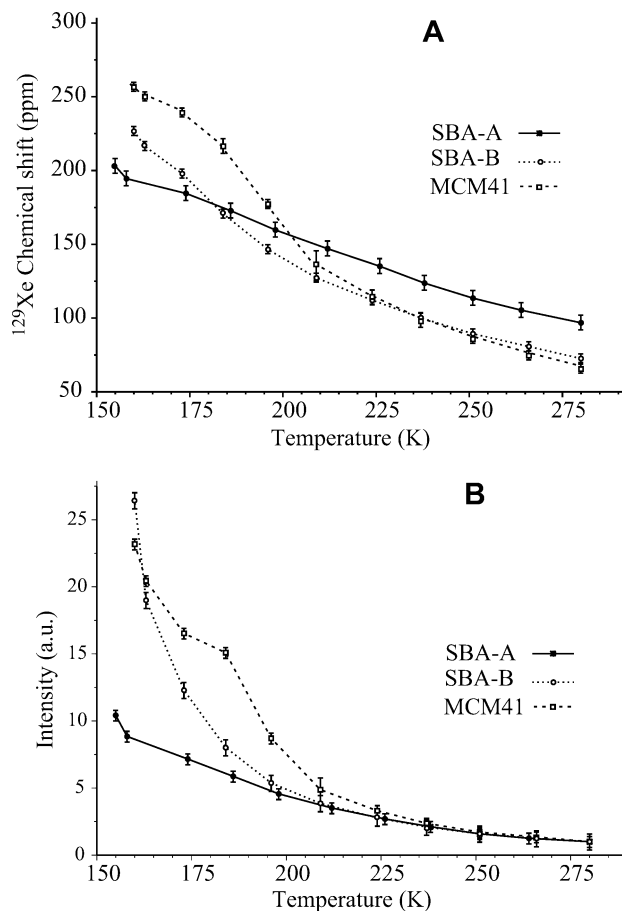


**Figure 3.** Chemical shift (A) and integrated intensity (B) of the main peak observed on the variable temperature  $^{129}\text{Xe}$  NMR spectra of MCM-41, SBA-A, and SBA-B silicas (upon cooling from room temperature down to 155 K, method A): (solid line, ■) SBA-A; (dotted line, ○) SBA-B; (dashed line, □) MCM-41.

SBA-B, are too steep to be due to the Boltzmann factor alone. The temperature dependences of the xenon chemical shift for MCM-41, on one hand, and for SBA-A and SBA-B, on the other hand, are quite different.



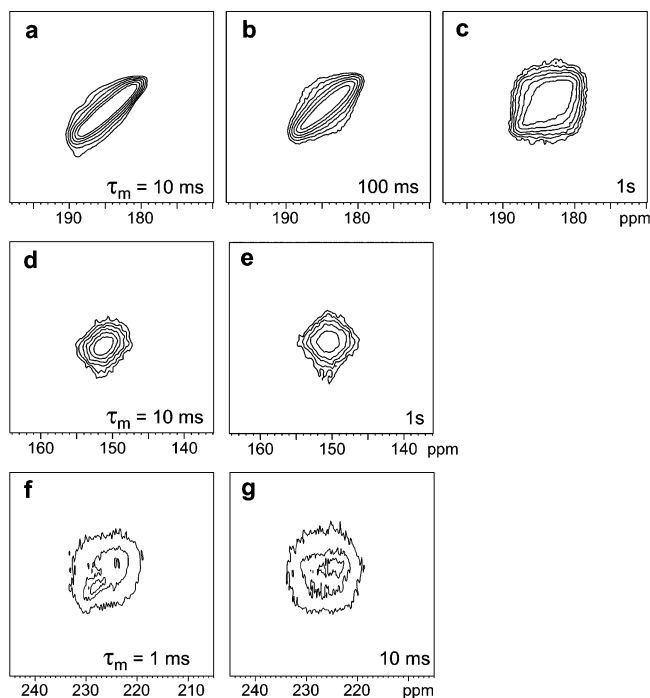


**Figure 4.** Contour plot expansions of 2D EXSY spectra measured at 190 K (a,b,c) on SBA-A, at 205 K (d,e) on SBA-B, and at 178 K on MCM-41 (f,g). The mixing time,  $\tau_m$ , is indicated in the lower right corner of each frame.

Let us summarize first the information obtained on MCM-41. For this silica, the spectra only display a symmetrical peak from room temperature down to 225 K. Only one adsorption site or very rapidly exchanging ones are thus detected. This peak, symmetrical above 225 K, becomes asymmetrical between 225 and 175 K (at least 30 min of equilibration at each temperature), but the symmetry is restored below 175 K. This indicates that the asymmetry observed in the intermediate temperature range is not due to instrumental heterogeneities such as temperature or field gradients. This asymmetry instead reveals overlapping peaks and confirms the presence of rapidly exchanging sites. Accordingly, on EXSY spectra acquired at 178 K, a square pattern is observed on the contour plot corresponding to mixing times of 1 and 10 ms (Figure 4f,g). Moreover, the appearance of an asymmetrical resonance on variable temperature spectra is accompanied by a sharp variation of the xenon signal intensity (Figure 3B). This intensity increase suggests that xenon condensation has begun, as independently confirmed by the chemical shift observed at 155 K, 252 ppm, which agrees well with that proposed by Pietrass et al.<sup>34</sup> for liquid xenon. Xenon condensation therefore occurs at temperatures significantly higher than those required in the absence of silica. Xenon must then be confined inside the mesopores because MCM-41 has no micropores. Therefore, physisorbed and condensed xenon coexist in the mesopores of MCM-41 between 225 and 175 K. Note that a very similar effect has already been observed by calorimetric and IR measurements in the case of water adsorption.<sup>35</sup> Finally, we have checked by IR that H-bonded silanols are fully eliminated after dehydration (data not shown). The silica surface of our MCM-41 silica is then made either of isolated silanols or of siloxanes bridges, corresponding, respectively, to hydrophobic and hydrophilic sites. On the most hydrophilic sites, the xenon interaction with the surface is most probably weak and xenon–xenon interactions may dominate the xenon adsorption energy, which explains why xenon condensation can be detected.

Let us now analyze the results obtained for SBA-15 silicas. For SBA-B, the sigmoidal behavior of the curve showing the main peak chemical shift versus temperature (Figure 3A) is less pronounced than that for MCM-41, and the signal intensity strongly increases at temperatures far below 200 K (Figure 3B). For SBA-A, the chemical shift curve is almost flat, and no sharp increase of the signal intensity is observed. Finally, at the lowest temperature used here (155 K), the main resonance is located at 225 ppm on SBA-B and 201 ppm on SBA-A. These two values are far from that expected for liquid xenon. Furthermore, at this temperature, there is an inversion of chemical shift values compared to the sequence of mesopore diameters:  $D_{\text{BJH}} \text{MCM-41} < D_{\text{BJH}} \text{SBA-A} < D_{\text{BJH}} \text{SBA-B}$  (Table 1). Moreover, this order is also opposite to that observed at room temperature. The inversion cannot be explained by differences of xenon loading for the three silicas, which should lead to the same asymptotic chemical shift value at low temperature. This inversion consequently results from a variation of the interaction potential between xenon and the surface, indicating that the hydrothermal treatment increases the xenon affinity for the silica surfaces.

All of these observations (particularly the intensity curves displayed in Figure 3B) prove that physisorbed and condensed xenon coexist in the mesopores of MCM-41 between 225 and 175 K, whereas xenon is completely condensed at 155 K. In contrast, xenon condensation in the mesopores of the SBA-15 silicas is only partial at the same temperature. This difference cannot be ascribed to the large mesopore diameters of SBA-15 because complete xenon liquefaction has already been reported for a mesoporous silica of larger mesopore diameter (118 Å, pressure of 5 bar).<sup>23</sup> This suggests instead that xenon–surface interactions are strong enough to hamper xenon condensation and that the related energetic term dominates the chemical shift. This is consistent with results of experiments performed at various xenon loadings on mesoporous silicas obtained by a sol–gel process<sup>34</sup> and with the calculation of  $^{129}\text{Xe}$  chemical shifts as a function of interatomic potentials.<sup>36</sup>

The resonance line widths of SBA-A and SBA-B differ significantly (1.15 kHz and 0.53 kHz, respectively, at 190 K). To understand this difference and to probe heterogeneities of xenon adsorption sites, 2D EXSY spectra were acquired at the temperature at which the small peak appears (190 K) and at the temperature corresponding to the maximum slopes observed in Figure 3A,B ( $\sim 205$  K). At 190 K, for SBA-A (Figure 4a–c), the shape of the main resonance changes with the mixing time. Elongated and diagonal at short mixing times (10 ms), this shape becomes more rounded at longer mixing times. This indicates that the line width can be attributed to heterogeneities of adsorption sites and that diffusion of xenon among these sites is slow. For SBA-B (Figure 4d–e), contour plots appear squared at all mixing times, indicating a much faster exchange process. Compared to SBA-B, more interaction sites or sites of larger interatomic energies are found on the mesopores surface of SBA-A. The aspect of the 2D EXSY spectra and the fact that the line width of the main peak observed with SBA-A is broader than that with SBA-B cannot be explained by a dispersion in mesopore diameters. Indeed, mesopore polydispersity is irrelevant because the width of the BJH mesopore distribution, calculated from the desorption branch of the  $\text{N}_2$  sorption isotherms, is even narrower on SBA-A than on SBA-B.<sup>17</sup> The differences observed between SBA-A and SBA-B rather reveal that the hydrothermal treatment reorganizes hydrophilic/hydrophobic domains within the mesopores because the interactions between xenon and surfaces mainly involve hydrophobic

forces. In other words, the hydrothermal treatment leads to a less "rough" mesopore surface, at least at the length scale that is probed by xenon.

**Small Peak Observed at Low Temperature for SBA-A and SBA-B.** The small peak, which is clearly detected at low temperature for SBA-A and SBA-B silicas of bimodal porosity, is not observed for an MCM-41 of unimodal porosity. This is a first and strong indication relating it to micropores.

For SBA-A, the small peak appears at 189 K with a chemical shift equal to 215 ppm. The temperature at which this peak appears, first established by cooling using method A (Figure 2), has been confirmed by using method B (see Supporting Information, Figure S1). With decreasing temperature, the chemical shift of this peak increases and reaches 240 ppm at 155 K. Here again, this chemical shift is compatible with that proposed by Pietrass et al. for liquid xenon (near 250 ppm).<sup>34</sup> The observation of liquid xenon at 189 K, that is, at nearly 20 K above the condensation temperature observed in the absence of silica (170 K), implies again a confinement effect. We assign therefore the small peak to xenon condensing in intrawall micropores.

A similar small peak is observed for SBA-B at 155 K, indicating that this silica still contains micropores. By using N<sub>2</sub> sorption data of SBA-15, Galarneau et al.<sup>14</sup> have shown that the ratio of the microporous volume relative to mesoporous one drops from 1 to 0 when the temperature of hydrothermal treatment, applied 48 h, is increased from 35 to 140 °C. This reveals an improvement in silica wall compactness. By using the textural information given in Table 1 and by extending the calculation method recommended by these authors, we obtain a microporous volume of 0.35 cm<sup>3</sup>/g and also a mesoporous volume of 0.35 cm<sup>3</sup>/g for SBA-A compared to a microporous volume of 0.20 cm<sup>3</sup>/g and a mesoporous volume of 0.90 cm<sup>3</sup>/g for SBA-B. These values point to a 60% decrease of the microporous volume and confirm our previous exploitation of XRD peak intensities that revealed a 40% increase of the electronic density of the silica walls when a 373 K hydrothermal treatment is applied during 72 h.<sup>17</sup>

Note that, for SBA-B, the small peak cannot be detected above 170 K. Furthermore, despite the relative amounts of micropores in SBA-A and SBA-B silicas, the small peak assigned to liquid xenon is twice more intense for SBA-B (6%) than for SBA-A (3%). These two observations suggest either differences in micropores dimensions, as recently introduced in the literature,<sup>16</sup> or different potential interactions of xenon with silica surfaces.

## Conclusion

We have used <sup>129</sup>Xe NMR to probe the porosities of three well-ordered mesoporous silicas: an MCM-41 of unimodal porosity, used as a reference, and two SBA-15, labeled SBA-A and SBA-B, of bimodal porosity (containing both mesopores and micropores). At high temperature, <sup>129</sup>Xe spectra can be analyzed in terms of an exchange of xenon between sites located on all of the silica surfaces (in micropores and mesopores) and the gas phase. In contrast, at low temperature, exchange rates are slowed and salient features of the complex porosity of mesoporous silicas have been characterized.

A main peak, recorded for the three silicas, essentially reflects the behavior of xenon in mesopores. At 155 K, xenon mostly condenses in the mesopores of MCM-41, but condensation is quite restricted for both SBA-A and SBA-B. Moreover, in the studied temperature range, for SBA-A, a distribution of adsorption sites, a surface "roughness" inside the mesopores, is

revealed by 2D EXSY experiments. On SBA-B, this surface "roughness" is no longer detected. These differences show that the silica surface in mesopores is different in nature and in adsorption potential because surface defects are altered by hydrothermal treatment.

A well-resolved small peak, only observed at low temperatures for SBA-A and SBA-B, is the fingerprint of xenon condensing in micropores. First, its chemical shift at 155 K, near 250 ppm, is identical to that associated with liquid xenon in earlier studies. Second, its detection at 189 K on SBA-A, that is, at 20 K above the temperature of xenon liquefaction in the absence of silica, implies a confinement effect different in nature from the one evidenced in mesopores. Interestingly, this peak is not detected above 170 K for SBA-B, illustrating differences either in micropore dimensions or in interactions of xenon with silica surfaces.

However, because of rapid exchange processes, it is almost impossible to obtain an estimate of the microporous volume by using <sup>129</sup>Xe NMR. For similar reasons, other NMR experimental methods such as T<sub>1</sub> measurements did not help us to discriminate the physical properties of the adsorption sites that we have associated with these two peaks.

**Acknowledgment.** The authors thank G. D. Stucky and M. Breyse for their constant help and support. The French Research Ministry is acknowledged for financial support (Grant ACI#4103).

**Supporting Information Available:** Figure S1 showing spectra of xenon in the reference tube (no silica) and adsorbed on MCM-41, SBA-A, and SBA-B using method B (absolute temperature calibration, equilibration for more than 15 min) and Figure S2 showing contour plot expansion of a 2D EXSY spectrum measured at 170 K on SBA-A showing cross-peaks between signals assigned to mesopores (main peak at 190 ppm) and micropores (small peak at 225 ppm). This material is available free of charge via the Internet at <http://pubs.acs.org>.

## References and Notes

- (1) Liu, A. M.; Hidajat, K.; Kawi, S.; Zhao, D. *Chem. Commun.* **2000**, 1145.
- (2) Han, Y. K.; Stucky, G. D.; Butler, A. *J. Am. Chem. Soc.* **1999**, *121*, 9897.
- (3) Yang, P.; Wirmsberger, G.; Huang, H. C.; Cordero, S. R.; MacGeehee, M. D.; Scott, B.; Deng, T.; Whitesides, G. M.; Chmelka, B. F.; Buratto, S. K.; Stucky, G. D. *Science* **2000**, *287*, 465.
- (4) Yue, Y. H.; Gédéon, A.; Bonardet, J. L.; d'Espinose, J. B.; Fraissard, J. *Stud. Surf. Sci. Catal.* **2000**, *129*, 209.
- (5) Morey, M. S.; O'Brien, S.; Schwarz, S.; Stucky, G. D. *Chem. Mater.* **2000**, *12*, 898.
- (6) Liu, Z.; Sakamoto, Y.; Ohsuna, T.; Hiraga, K.; Terasaki, O.; Ko, C. H.; Shin, H. J.; Ryoo, R. *Angew. Chem., Int. Ed.* **2000**, *39*, 3107.
- (7) Tian, B.; Liu, X.; Yang, F.; Xie, S.; Yu, C.; Tu, B.; Zhao, D. *Adv. Mater.* **2003**, *15*, 1370.
- (8) Kumar, D.; Schumacher, K.; du Fresne von Hohenesche, C.; Grün, M.; Unger, K. K. *Colloids Surf., A* **2001**, *187–188*, 109.
- (9) Zhao, D.; Feng, J.; Huo, Q.; Melosh, N.; Frederickson, G. H.; Chmelka, B. F.; Stucky, G. D. *Science* **1998**, *279*, 548.
- (10) Ryoo, R.; Ko, C. H.; Kruk, M.; Antochshuk, V.; Jaroniec, M. *J. Phys. Chem. B* **2000**, *104*, 11465.
- (11) Kruk, M.; Jaroniec, M.; Ko, C. H.; Ryoo, R. *Chem. Mater.* **2000**, *12*, 1961.
- (12) Shin, H. J.; Ryoo, R.; Kruk, M.; Jaroniec, M. *Chem. Commun.* **2001**, *4*, 349.
- (13) Göltner, C. G.; Smarsly, B.; Berton, B.; Antonietti, M. *Chem. Mater.* **2001**, *13*, 1617.
- (14) Galarneau, A.; Cambon, H.; Di Renzo, F.; Fajula, F. *Langmuir* **2001**, *17*, 8328.
- (15) Galarneau, A.; Cambon, H.; Di Renzo, F.; Ryoo, R.; Choi, M.; Fajula, F. *New J. Chem.* **2003**, *27*, 73.

- (16) Choi, M.; Heo, W.; Kleitz, F.; Ryoo, R. *Chem. Commun.* **2003**, 1340.
- (17) Imperor-Clerc, M.; Davidson, P.; Davidson, A. *J. Am. Chem. Soc.* **2000**, *122*, 11925.
- (18) Liu, J.; Zhang, X.; Han, Y.; Xiao, F. S. *Chem. Mater.* **2002**, *14*, 2536.
- (19) Newalkar, B. L.; Choudary, N. V.; Kumar, P.; Kormanani, S.; Bhat, T. S. G. *Chem. Mater.* **2002**, *14* (1), 304.
- (20) Prangé, T.; Schiltz, M.; Pernot, L.; Colloch, N.; Longhi, S.; Bourguet, W.; Fourme, R. *Protein Struct., Funct., Genet.* **1998**, *30*, 61.
- (21) (a) Barrie, P. J.; Klinowski, J. *Prog. Nucl. Magn. Reson. Spectrosc.* **1992**, *24*, 91. (b) Bonardet, J. L.; Fraissard, J.; Gédéon, A.; Springuel-Huet, M. *Catal. Rev. Sci. Eng.* **1999**, *41*, 115. (c) Springuel-Huet, M. A.; Sun, K.; Fraissard, J. *Microporous Mesoporous Mater.* **1999**, *33*, 89.
- (22) Ripmeester, J. A.; Ratcliffe, C. I. *J. Phys. Chem.* **1990**, *94*, 7652.
- (23) Cros, F.; Korb, J. P.; Malier, L. *Langmuir* **2000**, *16*, 10193.
- (24) Terskikh, V. V.; Mondrakovski, I. L.; Breeze, S. R.; Lnag, S.; Ratcliffe, C. I.; Ripmeester, J. A.; Sayari, A. *Langmuir* **2002**, *18*, 5653.
- (25) Schacht, S.; Janicke, M.; Schuth, F. *Microporous Mesoporous Mater.* **1998**, *22*, 485.
- (26) Moudrakovski, I. L.; Terskikh, V. V.; Ratcliffe, C. I.; Ripmeester, J. A.; Wang, L. Q.; Shin, Y.; Exarhos, G. J. *J. Phys. Chem. B* **2002**, *106*, 5938.
- (27) Nossou, A.; Haddad, E.; Guenneau, F.; Gédéon, A. *Phys. Chem. Chem. Phys.* **2003**, *5*, 4473.
- (28) Nossou, A.; Habbad, E.; Guenneau, F.; Mignon, C.; Gédéon, A.; Grosso, D.; Babonneau, F.; Bonhomme, C.; Sanchez, C. *Chem. Commun.* **2002**, 2476.
- (29) Labouriau, A.; Pietrass, T.; Weber, W. A.; Gates, B. C.; Earl, W. L. *J. Phys. Chem. B* **1999**, *103*, 4323.
- (30) L'air liquide. *Gas Encyclopedia*, Elsevier: Amsterdam, 1976.
- (31) Bringkmann, D.; Carr, H. Y. *Phys. Rev.* **1966**, *150*, 174.
- (32) Cowgill, D. F.; Norberg, R. E. *Phys. Rev. B* **1972**, *6*, 1636.
- (33) Jeener, J.; Meier, B. H.; Bachmann, P.; Ernst, E. R. *J. Chem. Phys.* **1979**, 71.
- (34) Pietrass, T.; Kneller, J. M.; Assink, R. A.; Anderson, M. T. *J. Phys. Chem. B* **1999**, *103*, 8837.
- (35) Cauvel, A.; Brunel, D.; Di Renzo, F.; Garrone, F.; Fubini, B. *Langmuir* **1997**, *13*, 2773.
- (36) Jameson, C. J. *J. Chem. Phys.* **2002**, *116*, 8912.